Remote Sensing of Environment 319 (2025) 114642

Contents lists available at ScienceDirect

Remote Sensing of Environment

journal homepage: www.elsevier.com/locate/rse

Non-linear spectral unmixing for monitoring rapidly salinizing coastal landscapes

Manan Sarupria [a,*], Rodrigo Vargas [b], Matthew Walter [a], Jarrod Miller [b], Pinki Mondal [a,b]

[a] Department of Geography and Spatial Sciences, University of Delaware, Newark, DE 19716, USA
[b] Department of Plant and Soil Sciences, University of Delaware, Newark, DE 19716, USA

ARTICLE INFO

Editor: Zhe Zhu

Keywords:
Saltwater intrusion
Spectral Unmixing
Sentinel-2
Random Forest (RF)
Coastal agriculture

ABSTRACT

Coastal farmlands in the eastern United States of America (USA) are increasingly suffering from rising soil salinity, rendering them unsuitable for economically productive agriculture. Saltwater intrusion (SWI) into the groundwater reservoir or soil salinization can result in land cover modification (e.g. reduced plant growth) or land cover conversion. Two primary examples of such land cover conversion are farmland to marsh or farmland to salt patches with no vegetation growth. However, due to varying spatial granularity of these conversions, it is challenging to quantify these land covers over a large geographic scale. To address this challenge, we evaluated a non-linear spectral unmixing approach with a Random Forest (RF) algorithm to quantify fractional abundance of salt patch and marshes. Using Sentinel-2 imagery from 2022, we generated gridded datasets for salt patches and marshes across the Delmarva Peninsula, and the associated uncertainty. Moreover, we developed two new spectral indices to enhance the spectral unmixing accuracy: the Normalized Difference Salt Patch Index (NDSPI) and the Modified Salt Patch Index (MSPI). We constructed two sets of ten RF models: one for salt patches and the other for marshes, achieving high (>99 %) training and testing accuracies for classification. The consistently high accuracy and low error values across different model runs demonstrate the method's reliability for classifying spectrally similar land cover classes in the mid-Atlantic region and beyond. Validation metrics for sub-pixel fractional abundances in the salt model revealed a moderate R-squared value of 0.50, and a high R-squared value of 0.90 for the marsh model. Our method complements labor-intensive field-based salinity measurements by offering a reproducible method that can be repeated annually and scaled up to cover large geographic regions.

1. Introduction

Saltwater intrusion (SWI) is often a combined effect of relative sea-level rise (SLR), coastal storm surges, land subsidence, drought, and excessive groundwater pumping. With ongoing climate changes projected to further intensify some of these drivers over the next decades, SWI poses a critical threat to coastal ecosystems, leading to progressively diminishing soil health and compromised agricultural production (Tully et al., 2019a; Tully et al., 2019b; White et al., 2022). The impacts of SWI are increasingly evident on coastal agricultural land, where elevated soil salinity leads to farmland degradation and reduced crop yields (Corwin, 2020; Measho et al., 2022). Additionally, SWI is closely linked to the expansion of ghost forests (Kirwan and Gedan, 2019), conversion of productive farmlands into marshes, and upward marsh migration, (Campbell et al., 2022; Guimond and Michael, 2021; Mondal et al., 2023). Therefore, accurately detecting the impacts of SWI in coastal agricultural ecosystems is imperative to inform environmental management, as well as economic, and policy decisions (Amini et al., 2016; Omuto et al., 2012).

There is a need to develop robust and scalable methods to track the spatial extent of salt patches and marshes across large geographic areas to understand the impact of SWI on coastal ecosystems. Field- and laboratory-based methods can accurately quantify the degree of soil salinity at specific sites, but these are expensive and time-intensive when employed in large areas (Gallant, 2015; Metternicht and Zinck, 2003). Utilizing remote sensing data offers the most practical means of mapping and monitoring the impacts of SWI over large areas, providing land-surface information at medium-to-high spatial (100 m - 1 m) and high temporal resolutions (1 day - 5 days). Salt accumulation on bare soil creates patches with distinct spectral signatures, characterized by high

* Corresponding author.
E-mail addresses: manansar@udel.edu (M. Sarupria), rvargas@udel.edu (R. Vargas), mswalter@udel.edu (M. Walter), jarrod@udel.edu (J. Miller), mondalp@udel.edu (P. Mondal).

https://doi.org/10.1016/j.rse.2025.114642
Received 10 August 2024; Received in revised form 22 January 2025; Accepted 31 January 2025
Available online 7 February 2025

reflectance in the visible and near-infrared (VNIR) regions of the electromagnetic spectrum due to well-developed saline efflorescence, while the shortwave infrared (SWIR) region shows greater absorption due to higher soil moisture content, which is often linked to salt content differences (Mougenot et al., 1993).

Prior studies have focused on mapping the spatial distribution of salt-affected soils with varying levels of accuracy and spatial coverage, spanning from local to global scales (Hassani et al., 2021; Montanarella et al., 2015; Scudiero et al., 2014). For example, multispectral remote sensing images, such as those from Sentinel-2 and Landsat 8, have been explored for soil salinity detection (Bai et al., 2016; Bannari et al., 2018; Davis et al., 2019). Bannari et al. (2018) concluded that Sentinel-2's SWIR bands are excellent candidates for integrating soil salinity modeling and monitoring at various scales, using a combination of remote sensing data and field measurements of soil pHs, electrical conductivity, major soluble cations and anions. Davis et al. (2019) compared the ability of Landsat 8 OLI and Sentinel-2 MSI to estimate electrical conductivity (EC), finding that visible spectral bands, especially in the blue and red ranges, were sensitive to soil salinity, although both sensors showed low overall accuracies, highlighting the need for narrowband sensors. Bai et al. (2016) compared Landsat 8 Operational Land Imager (OLI) and Sentinel-2 Multispectral Imager (MSI) data, alongside field-collected soil physiochemical data, to identify key variables through physico-chemical, statistical, and spectral analysis for extracting soil alkalinity and salinity, noting that Sentinel-2's higher spatial resolution provided more accurate salinity mapping. Other studies have utilized the potential of combining vegetation and soil indices such as normalized difference vegetation index, bare soil index, vegetation soil salinity index, soil adjusted vegetation index, spectral salinity index, and normalized differential salinity index (Alqasemi et al., 2021; Ennaji et al., 2018; Li et al., 2015; Nguyen et al., 2020). These indices are often used along with machine learning algorithms, including Random Forest (RF), to predict soil salinity (Hassani et al., 2021; Kaplan et al., 2023; Mondal et al., 2023; Zhang et al., 2022). Most studies use lab-derived electrical conductivity (EC) values to train salinity models by integrating remote sensing datasets. But the timing of soil sample collection for EC measurement has been shown to significantly influence modeled salinity levels due to seasonal fluctuations (Lam et al., 2022; Hossain and Li, 2024). Similarly, the dynamically changing extent of coastal marshes has been mapped and analyzed using spectral and structural attributes derived from high-resolution remote sensing data (Liu et al., 2017; Massetti et al., 2016; Qi et al., 2021). When trying to enhance classification accuracy by integrating field-based methods, several errors can be introduced during manual sample collection and laboratory measurements (Chesher, 1991). As a result, the scalability of those approaches to larger areas and with higher temporal resolution is constrained.

Mapping salt patches has additional challenges that stem from (i) their widely variable sizes, ranging from a few meters to hundreds of meters, (ii) spectral similarities in the visible spectrum arising from the white color of salt crusts on the soil surface, which can closely resemble other land features such as poultry litter or white farm tunnels, and (iii) the temporal changes in salt patch signatures (Corwin and Scudiero, 2019). High-resolution (1 m) aerial data from the National Agriculture Imagery Program (NAIP) has been used for effective salt patch mapping and change detection in this context (Mondal et al., 2023); however, the temporal resolution is limited due to the 2–3 year image acquisition interval for NAIP. Moderate to high spatial resolution (1–30 m) satellite and airborne imagery can still be affected by the abundance of mixed pixels, where a single pixel constitutes more than one land cover class. The presence of mixed pixels can introduce inaccuracies in differentiating different land cover classes (Mahdavi et al., 2018). Spectral characteristics of salt patch pixels vary due to soil type, texture, moisture content, and co-location of vegetation (crops or marsh plants). Similarly, mapping marshes presents innate challenges compared to other wetland vegetation due to their highly dynamic nature, variable species composition, and the spectral and backscatter similarities to other wetland vegetation (Gallant, 2015). Despite advancements in remote sensing of soil salinity and marsh mapping, a methodological gap remains for efficiently capturing these signatures over larger geographic areas at finer spatial and temporal scales.

This study aims to bridge this gap by producing gridded datasets at 10 m spatial resolution for salt patches and marsh on a larger geographic scale (>15,000 km^2) without using field/lab-derived soil salinity values. We achieved this by performing spectral unmixing on Sentinel-2 imagery (spatial resolution: 10 m, temporal resolution: 5 days) using the Random Forest (RF) classifier across 14 coastal counties of Delaware, Maryland, and Virginia (the Delmarva Peninsula). Sentinel-2 images exhibit superior spatial and temporal resolutions in comparison to Landsat (Davis et al., 2019) and have been utilized successfully for monitoring surface soil salinity and assessing soil management (Ramos et al., 2020; Taghadosi et al., 2019). Yet, the spatial resolution of Sentinel-2 images (10-20 m for VNIR bands) is not sufficient enough to accurately capture scattered salt patches. Employing spectral unmixing addresses this limitation by quantifying the abundance fractions of multiple endmembers within a pixel. This approach determines the proportion of area covered by each desired land cover class for individual pixels, thereby enhancing the accuracy of the resulting map (Bouaziz et al., 2020; Cruz et al., 2019; Masoud et al., 2019; Racoviteanu et al., 2021). To further enhance the classification approach, we developed two novel salinity indices in this study that aim to increase the spectral separability between bare soil and salt patch classes.

Understanding SWI dynamics at a high spatiotemporal resolution is critical for sustainable land management in the face of climate change. However, it is equally important to understand the level of uncertainty associated with the results produced by machine learning models for their reliability in decision making (Atkinson and Foody, 2002; Hsiao and Cheng, 2016). Furthermore, assessing the quality of input data used for model training is critical to determine its representativeness for the study area. To address the reliability and applicability of our model, we quantified the uncertainty associated with spectrally unmixed maps of salt patches and marshes. Additionally, we evaluated RF's sensitivity to changing input data volumes. The primary research questions addressed in this study are as follows:

1) How can spectral unmixing of Sentinel-2 imagery be effectively employed to accurately map the extent of salt patches and marshes in Delmarva in 2022?
2) Which spectral indices and/or image bands are most effective for capturing salt patch signals?
3) What is the range of uncertainty associated with the predicted values of the spectrally unmixed pixels of salt patches and marshes?
4) How does the RF model respond to varying amounts of input data?

Overall, this study provides a novel contribution to geospatial monitoring of coastal landscapes facing SLR because of its reduced dependence on lab-derived soil salinity values, the scalability of our approach, and the potential for high-resolution near-real-time information produced by the RF model.

2. Study area

The Delmarva Peninsula contains at least 35 % of its land within a vertical proximity of 5 m to the high tideline (Titus et al., 2009; Fig. 1). The Peninsula covers a total land area of 15,670 km^2. The region is bordered by Chesapeake Bay to the west, Delaware Bay, and the Atlantic Ocean to the east, which regulate temperature and bring moisture landward. However, the region contains multiple regional climates, where the southern and eastern parts of the peninsula tend to have mild temperatures and wetter conditions, and the northern and western parts tend to have cooler temperatures and drier conditions. Delmarva is mainly characterized by marshes and agricultural lands. Agriculture and

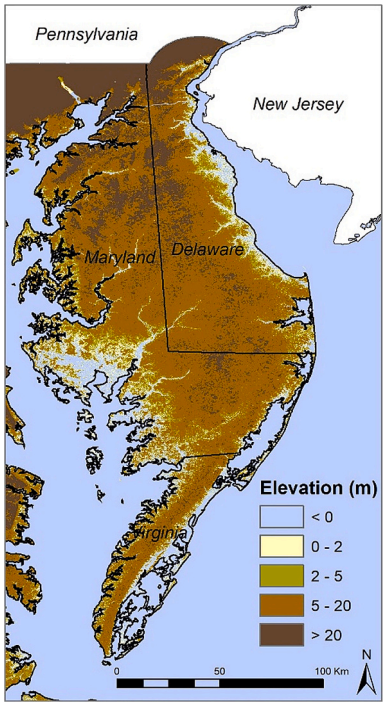

Fig. 1. Map of the study area, the Delmarva Peninsula, spanning 14 coastal counties of Delaware, Maryland, and Virginia. Colors show the range of elevation above mean sea level.

aquaculture are the backbone of the region's economy, with seafood, poultry, corn, and soybeans as vital components.

3. Materials and methods

In this study, we employed a multi-sensor and multi-resolution approach. This approach integrated Sentinel-2 Level 2 A surface reflectance imagery, a global land use/land cover dataset from ESRI (Karra et al., 2021), a NAIP-derived Delmarva land cover dataset (Mondal et al., 2022), high-resolution PlanetScope true color images (Planet Team, 2017), very high-resolution Unoccupied Aerial Vehicle (UAV) imagery, and ground truth data. These diverse datasets were included in a machine learning classification method, and different testing and validation approaches were used to ensure the accuracy and reliability of the analysis.

3.1. Remotely sensed data

Spectral unmixing was conducted on publicly available Sentinel-2 Level 2 A surface reflectance imagery, a multispectral dataset corrected for atmospheric effects and radiometric errors, with 13 spectral bands spanning visible to near-infrared regions of the electromagnetic spectrum (0.443–2.190 μm). These images have a range of spatial resolutions from 10 m to 60 m and are acquired every 5 days. Sentinel-2 Level 2 A imagery has been widely used in land use/land cover mapping, vegetation monitoring, and crop yield estimation (Pesaresi et al., 2016; Phiri et al., 2020; Sibanda et al., 2015; Sitokonstantinou et al., 2018). We used very high-resolution (60 cm) images of selected farmlands in Dorchester and Somerset counties in Maryland using UAV to facilitate the selection of reference points for model training and testing. UAV imagery was acquired on sunny or consistently overcast days when the sun was greater than 30° above the horizon. A DJI (Shenzhen, China) Inspire 2 equipped with a DJI 24 mm Zenmuse camera was flown 120 m above ground level with 75 % side and front overlap. Before the flight, ground control points (GCPs) were marked using an Emlid (Budapest, Hungary) Reach RS2+ RTK GPS receiver using the EGM2008 Geoid for elevation. Pix4DMapper (Prilly, Switzerland) was used to mark GCPs and stitch imagery into orthomosaics using the default settings for processing RGB imagery. We used Sentinel-2 derived global land use/land cover dataset to filter pertinent land cover classes such as 'Crops' and 'Rangeland' (Karra et al., 2021). Additionally, a NAIP-derived Delmarva land cover dataset (Mondal et al., 2022, 2023) with eight classes was used to mask out non-agricultural land cover classes such as 'Built' and 'Forest'. This classification, derived using an RF algorithm with 94,240 reference points (used for training and testing the model), had 85–91 % overall accuracy and Kappa values exceeding 0.8 (Mondal et al., 2023). Lastly, high-resolution PlanetScope true color images, offering 3-5 m spatial resolution and daily temporal coverage, served as reference data for for model validation (Planet Team, 2017). Fig. 2 shows a flowchart summarizing the methodological workflow of this study, incorporating all the data.

3.2. Pre-processing: NDVI maximum composite and spectral indices

A composite image was created from a collection of Sentinel-2 Level 2 A imagery, utilizing a maximum Normalized Difference Vegetation Index (NDVI) filter (Holben, 1986; Roy, 2000). The composite image was developed using a series of Sentinel-2 images from June 1–August 30, 2022. From this stack, pixels from the date with the maximum NDVI values were retained in the final composite. Cropland areas with excessively high salinity levels will have reduced or no crop cover, even at the peak of the growing season, which will be retained in the NDVI maximum composite image. Sentinel-2 cloud probability imagery was used to perform cloud masking over each layer with a 20 % threshold for the maximum cloud probability. The pre-processing of Sentinel-2 imagery was performed on a cloud-based geospatial data processing platform, Google Earth Engine (GEE).

The NDVI maximum composite included seven original Sentinel-2 bands (B2, B3, B4, B5, B6, B8, B11). The red-edge band 7, while informative, was omitted as the red-edge bands B5 and B6 alone provide sufficient spectral information for this study's objectives (Wang et al., 2019). Band 8 (broadband NIR, 0.842 μm) was preferred over Band 8a (narrow-band NIR, 0.865 μm) due to its higher spatial resolution (10 m vs. 20 m) and minimal differences in spectral reflectance (Fernandez-Manso et al., 2016; Navarro et al., 2017). For SWIR, Band 11 (SWIR-1, 1.61 μm) was selected over Band 12 (SWIR-2, 2.19 μm) due to its slightly stronger correlation with soil moisture, which is critical for distinguishing saline soils (Hegazi et al., 2023; Sadeghi et al., 2015; Shokati et al., 2024). This combination minimized redundancy while enhancing the study's accuracy. Bands 5, 6, and 11 (20 m resolution) were resampled to 10 m resolution using nearest neighbor sampling in Google Earth Engine (GEE) to align them with the other bands. Nearest neighbor resampling, applied through functions like "addBands", ensures consistent pixel alignment while preserving the spectral integrity of the data.

Additionally, the NDVI maximum composite consisted of five indices, including Enhanced Vegetation Index (EVI; Huete et al., 2002), Moisture Stress Index (MSI; Ceccato et al., 2001; Hunt and Rock, 1989), and Modified Soil Adjusted Vegetation Index (MSAVI; Qi et al., 1994) (Table 1). Highly saline soils often exhibit sparse vegetation and lower NIR band reflectance, similar to bare soil. It is known that EVI and MSI directly gauge vegetation growth and health, which are affected by salinity changes. MSAVI mitigates soil background noise, which is crucial for accounting noise in pixels with high soil brightness. Additionally, we developed the Normalized Difference Salt Patch Index (NDSPI) and Modified Salt Patch Index (MSPI) to enhance spectral separability between salt and bare soil classes. These indices were calculated based on the average spectral reflectance plots of salt patches and bare soil (SI Fig. 1). These new indices were developed in this study to maximize the difference in values between salt patches and bare soil. Collectively these five indices offer crucial information on the presence of surficial salinity.

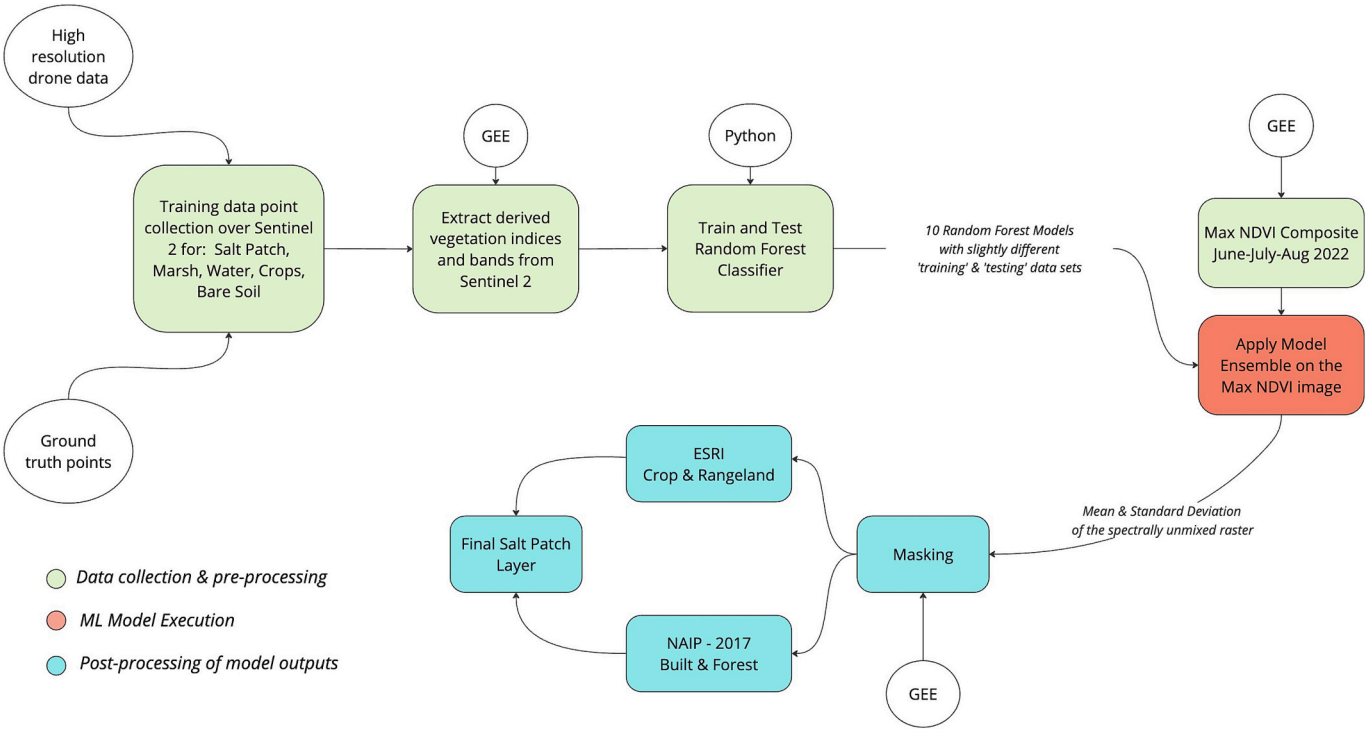

Fig. 2. Flowchart illustrating the data processing and modeling methodology.

Table 1
Spectral indices, including two new indices developed in this study, derived from Sentinel-2 spectral bands to aid in spectral unmixing.

Spectral Index	Equation	Reference
EVI: Enhanced Vegetation Index	$2.5 \times \frac{(NIR - RED)}{(NIR + 6 \times RED - 7.5 \times BLUE + 1)}$	Huete et al., 2002
MSAVI: Modified soil-adjusted vegetation index	$\frac{2 \times NIR + 1 - \sqrt{\left((2 \times NIR + 1)^2 - 8 \times (NIR - RED)\right)}}{2}$	Qi et al., 1994
MSI: Moisture Stress Index	$\frac{SWIR}{NIR}$	Ceccato et al., 2001; Hunt and Rock, 1989
NDSPI: Normalized Difference Salt Patch Index	$\frac{SWIR - B}{SWIR + B}$	Generated in this study.
MSPI: Modified Salt Patch Index	$\frac{R + G + B + NIR - SWIR}{R + G + B + NIR + SWIR}$	Generated in this study.

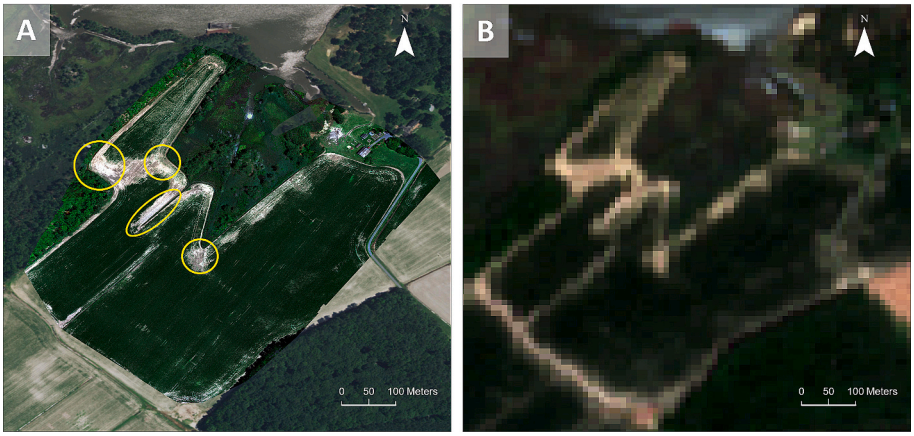

Fig. 3. True color images revealing saltwater intrusion effects on farmland: (A) High-resolution UAV image of the farmland (60 cm resolution) overlaid on NAIP imagery in the background (1 m resolution) with yellow circles highlighting locations of salt patch; (B) Sentinel-2 true color image (10 m resolution). (For interpretation of the references to color in this figure legend, the reader is referred to the web version of this article.)

3.3. Reference data for RF model training

For training, we selected five prevalent endmembers—salt patch, bare soil, crop, water, and marsh—found in and around selected farmlands. Reference points for bare soil are pixels of soil on farmlands with no salt patch and no crops. Reference points for salt are pixels of salt patches over bare soil with minimal to no vegetation. Reference points were collected using Sentinel-2 imagery, primarily captured on June 29th, 2022, and supplemented by additional UAV imagery from various dates (Fig. 3A). Farm locations were selected based on prominent salt patch visibility, with dates closest to the UAV flight date. Additional land cover ground truth data were collected in the summer of 2022 to complement the remotely collected points (Fig. 3B). A total of 27,437 reference points (salt = 239, bare soil = 1096, crop = 5198, water = 20,131, and marsh = 773) were collected for training and testing the models. Out of >27,000 reference points, 142 (salt = 69, bare soil = 23, and crop = 50) were collected during field visits, while the rest were collected digitally with visual assistance from PlanetLabs data.

3.4. Spectral Unmixing method

Spectral unmixing determines the fraction of the area covered by multiple endmembers in a mixed pixel (Adams et al., 1986; Smith et al., 1990). Mixed pixels can occur for two reasons. First, a sensor's coarse spatial resolution captures spectral signatures of multiple endmembers within one pixel. Second, when multiple endmembers are physically present in close association, they may exist as a homogeneous mixture.

Spectral unmixing can be performed through two mathematical approaches: linear and nonlinear (Keshava et al., 2000). Linear spectral unmixing assumes the mixed pixel's spectral signature as a linear combination of its constituent endmembers (Fig. 4). Using the least squares error method, the observed reflectance is derived by combining endmember reflectance to minimize squared errors (Boardman, 1994). This method becomes more robust when endmember constituents are spatially proximate rather than well-separated. In such cases, predicting the reflectance of a mixed pixel through a linear combination of individual endmembers' spectral signatures may yield inadequate results. This limitation emphasizes the necessity for more sophisticated nonlinear models in scenarios where endmember distributions overlap or are closely situated, enhancing the accuracy of spectral unmixing.

3.5. Spectral Unmixing using RF

In this study, we used a Random Forest (RF) classifier for nonlinear spectral unmixing. While an RF regressor might seem suitable for predicting continuous variables like fractional abundance, we opted for the classifier for several reasons. The primary difference between the two approaches is that the RF regressor predicts continuous values, whereas the classifier assigns categories. For spectral unmixing, an RF regressor could potentially predict the exact fractional abundance of each endmember (ranging from 0 to 1). However, this approach requires a large amount of high-quality, continuous training data with diverse examples, which was difficult to obtain in our case. Collecting data for a full range of salt patch fractional abundance was particularly challenging due to field access issues and the limited number of pure salt patch samples, 239 in this case.

Given these challenges, the RF classifier was a better choice because it performs well with limited, noisy, and imbalanced training data, and is widely used for land cover mapping due to its robustness against overfitting and its ability to handle noisy input efficiently (Belgiu and Drăguţ, 2016). The RF classifier operates on an ensemble of decision trees, independently trained on random subsets of training data using bootstrap aggregation (Lee et al., 2020). Aggregating votes from all trees determine the final output, assigning the end member with the highest aggregated votes as the ultimate decision. To access the soft voting information, we used the Random Forest (RF) classifier's probability prediction function, 'predict_proba'. This function allows each decision tree to generate a probability distribution for each endmember, rather than making a single class decision. The probability distribution from a decision tree reflects the likelihood of an input pixel belonging to each endmember. The final predicted probabilities are obtained by averaging these probability distributions across all decision trees for each of the five endmembers. Consequently, each pixel in the final output is represented by five probability values, each indicating the fractional abundance of the corresponding endmember within that pixel (Licciardi and Del Frate, 2010). These probabilities sum to one, effectively depicting the spectral unmixing of a mixed pixel. A pixel value of 0 indicates the absence of a specific endmember, while 1 indicates a pure pixel. All values between 0 and 1 indicate varying levels of mixed endmembers. We employed a RF classifier with 100 trees, applying the 'balanced subsample' argument for class weight, keeping other parameters at the default value (max depth: None, min_samples_split: 2,

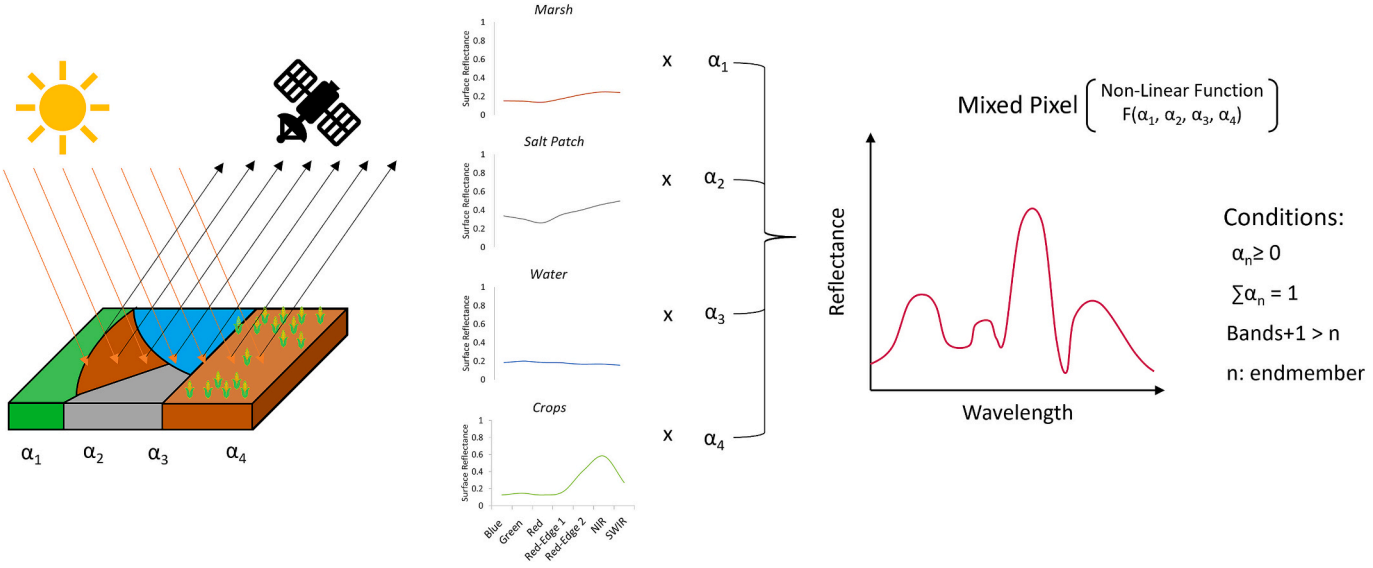

Fig. 4. Spectral unmixing of a mixed pixel with randomly arranged multiple endmembers (land cover classes) reveals individual pure endmembers' reflectance, deconvoluted based on their fractions α1, α2, α3, α4 within the pixel area, while adhering to the mathematical boundary conditions.

min_samples_leaf: 1). The 'balanced subsample' addresses uneven training sample distribution among different classes to ensure balanced representation during model training. Python coding language was used to perform all the above operations.

3.5.1. Spectral unmixing of salt and marshes

The study focuses primarily on the spatial extent of the salt patch and marshes. To make robust predictions, two separate RF models were trained, one with a focus on predicting salt patches and another for marshes. The models differ in the amount of training data used and distribution of reference points in each class. The RF model for salt patch unmixing consisted of a total of 4302 reference points, i.e. 239 for salt patch, 1195 for crop, and 956 points each for bare soil, water, and marshes. Due to the scarcity of salt-only pixels for accurate ground truthing, fewer salt pixels were collected for training compared to other classes. We used a subset of reference points from different classes for the salt patch RF model to maintain a training balance across classes. The RF model for marsh unmixing consisted of all the reference points, i.e. 239 for salt patch, 5198 for crop, 1096 for bare soil, 20,131 for water, and 773 for marshes. For both models, the input data was split into 80 % for training and 20 % for testing.

The fractional abundance image for the salt patch layer was extracted from the output of the RF classifier by selecting pixels with values equal to or greater than 0.4, and a threshold was chosen based on acceptable range of standard deviation for the predicted values to ensure a high level of certainty. Subsequently, the marsh layer was extracted from the unmixed output using a pixel value threshold greater than or equal to 0.25.

We applied a masking method to exclude irrelevant land cover classes from the final salt and marsh layer analysis. Focusing specifically on salt layers atop farmland and rangeland, we employed the 'Crop' and 'Rangeland' classes from the Sentinel-2 derived global land use land cover dataset (Karra et al., 2021). To mitigate misclassifications stemming from the Sentinel-2 classification's 10 m resolution, potentially mistaking narrow roads and small roofs within farmland perimeters as 'Cropland,' we integrated the 2016–2017 National Agriculture Imagery Program (NAIP)-derived 'Built' class from Mondal et al. (2023) as a mask. Upscaling the NAIP classified map to a 10 m resolution was achieved via the aggregate function in ArcGIS Pro, consolidating 1 m × 1 m NAIP pixels into 10 m × 10 m squares. Additionally, we utilized the 'Forest' class from Mondal et al. (2023) dataset to exclude land cover classes not of interest for this study, ensuring a focused analysis of pertinent regions. Subsequently, to enhance the accuracy of the 'Marsh' layer, the 'Built' and 'Forest' classes from Mondal et al. (2023), alongside 'Built' and 'Cropland' classes from Sentinel-2 global land use land cover map (Karra et al., 2021), were used for refined masking to rectify potential misclassifications. This masking procedure was executed on GEE.

3.6. RF model performance, uncertainty assessment and sensitivity analysis

The RF model performance was assessed using the training and testing accuracy values. Additionally, three extensively employed metrics including precision, recall, and the F1 score were calculated to evaluate model performance (Blagec et al., 2020) using the "classification_report" function from the metrics module of the Scikit-learn python library. Precision measures the proportion of true positive outcomes among all positive predictions, indicating the model's ability to minimize false positives. A higher precision score indicates a lower rate of false positives. Recall measures the proportion of actual positive instances correctly identified by the model, reflecting its ability to minimize false negatives. A higher recall score indicates a lower rate of false negative results. The overall performance of the multivariable binary classification model is represented by the F1 score, which is calculated as the harmonic mean of precision and recall. A score of 1 indicates perfect precision and recall, whereas a score of 0 indicates poor model performance. Additionally, the k-fold cross-validation was applied in this study by splitting the dataset for model training and testing into five equal-sized subsets. This was done using the "cross_val_score" function and the KFold class from the "sklearn.model_selection" module in the Scikit-learn python library. The model was trained and evaluated five times, each iteration using a different subset as the validation set and the remaining subsets as the training set. The "cross_val_score" function was then used to evaluate the performance of the Random Forest classifier on each fold, producing accuracy scores for all five folds. This process allows for a more rigorous assessment of the stability of the model performance by reducing the dependency on a single train-test split.

First, a total of 988 pixels (227 and 761 Sentinel-2 pixels for salt and marsh respectively), representing a range of fractional abundance were identified. Then, multiple high-resolution (3 m) PlanetScope images from August 13, 2022, were overlaid on Sentinel-2 images to collect validation points through a visual assessment. For each of those 988 Sentinel-2 pixels, fractional abundance were computed for salt patch and marsh by counting the number of PlanetScope pixels within each Sentinel-2 pixel and converting that to a fractional abundance. It is important to note that the Sentinel-2 and PlanetScope pixels don't align perfectly (SI Fig. 2), thus requiring an approximation for these fractional abundance values. Based on these observed fractional abundances from the visual assessment, we then computed multiple error matrices, including mean absolute error (MAE), mean square error (MSE), root mean square error (RMSE), and R^2 (Table 4). MAE represents the average of the residuals, MSE measures the variance of the residuals, RMSE indicates the standard deviation of the residuals, and R^2 determines the percentage of variance in the dependent variable explained by the variance in the independent variable.

To further assess model uncertainty, we focused on how the variability of the input training data influenced model outputs. For this, two sets of RF models were created, one for predicting salt patch and another for marsh, each comprising 10 RF models. The input reference data for these models were split into training and testing sets at an 80 %–20 % ratio. The split was repeated ten times on both the salt RF model reference data and the marsh RF model reference data without a fixed random state. This variation in training and testing data across runs enhances the robustness of decision tree ensembles, mitigating overfitting risks. Diverse decision trees accommodate various data aspects, reducing the impact of outliers or noise and effectively handling different scenarios. The mean and standard deviation were computed for each pixel in the final layer, offering insight into the sensitivity of the model to the input training data and the amount of variability in the model output.

We evaluated the RF model's sensitivity to different amounts of training data to determine if the input data appropriately represents the heterogeneity in the study area. To gauge this, we reduced the total data points by half for the salt and marsh RF models in both training and testing sets compared to the original dataset. Subsequently, we repeated the previously mentioned procedures. To measure sensitivity, we assessed the standard deviation of predicted values of the abundant fractions within distinct ranges—specifically, between 0.4 and 1 for salt patch and 0.25 to 1 for marsh. We then compared these results with model runs that utilized the entire dataset.

3.7. Variable importance factor

To improve model interpretability and evaluate the relative significance of various input variables, including bands and indices, we performed a variable importance factor (VIF) analysis using the Python package 'feature_importances_'. This factor quantifies the impact of each variable on overall classification accuracy. Two main methods for calculating the VIF from RF models include the out-of-bag error method and the Gini impurity method. In this study, we used the Gini impurity method (Breiman, 2001; Hastie et al., 2009). The importance of each

variable is determined by measuring the change in predictive accuracy when that variable is randomly altered, while keeping all others constant. If modifying a variable significantly improves the model's predictive accuracy, the variable holds substantial relative importance.

4. Results

In this section, we present the results of our study, which explores the application of Random Forest to perform spectral unmixing using Sentinel-2 imagery to accurately map the extent of salt patches and marshes in Delmarva for the year 2022. Our findings highlight the effectiveness of specific spectral indices and image bands in capturing the unique signals associated with salt patches. Additionally, we assess the uncertainty related to the predicted values of spectrally unmixed pixels, as well as how variations in input data influence the performance of our random forest model. Overall, this research contributes to advancing geospatial monitoring of coastal landscapes affected by sea-level rise, offering a scalable approach that minimizes reliance on laboratory-derived soil salinity measurements while enabling high-resolution and near-real-time assessments.

4.1. RF model performance assessment

4.1.1. Model accuracy and cross-validation

The ten salt patch RF classifiers achieved an average training and testing accuracy of 100 % and 99.8 %, respectively, while the marsh classifiers achieved 100 % and 99.9 %. The salt unmixing model outperformed the marsh unmixing model in terms of F1 score for salt classification, while the marsh model surpassed the salt unmixing model in F1 score for marsh classification (Table 2). This justifies our choice to develop two distinct models specialized in identifying salt and marsh areas. The model performance metrics, including precision, recall, and F1 score of 1, demonstrated excellent performance for crop unmixing in both the salt and marsh unmixing models. However, the precision and recall scores for the bare soil, 0.996 and 0.997, respectively, and for the salt, 0.991 and 0.988, respectively, were slightly below 1 for the salt unmixing model.

The k-fold cross-validation with 5 folds yielded an accuracy of 99.8 % and 99.9 % on average, for the salt and marsh unmixing models respectively (Table 3). These results underscore the models' robust performance on unseen data, suggesting their strong potential for reliable application in real-world scenarios.

Visual validation of the model's predictions was close to the model-derived values for salt unmixing, as evidenced by low MSE and MAE values of 0.035 and 0.059, respectively (Table 4). However, the model does not explain all the variability in the data, as evidenced by the moderate R-squared value of 0.50. While the model is performing well in prediction accuracy, there may still be room for improvement in explaining the underlying variability in the data.

The root mean squared error (RMSE) of 0.186 further indicated relatively low variability around the mean error, suggesting consistency in model performance. All performance metrics for marsh unmixing indicated good model performance. The spectral unmixing performances of the salt and marsh models are illustrated in Fig. 5, which presents a high-resolution true-color image from PlanetScope alongside the spectrally unmixed outputs from Sentinel-2 for the same area, highlighting the fractional abundance of salt patches and marsh regions. The area estimation for total salt patch and marsh extent was calculated by summing the fractional values across all pixels for each land cover class, following post-processing and masking, and multiplying by 10^{-4} to convert the area to km^2. The total estimated area of Delmarva covered with salt patches and marshes, based on the cumulative mean values from ten RF models, was found to be 14.43 km^2 and 1119.16 km^2, respectively.

Table 2
Mean precision, recall, and F1 score from 10 models for salt and marsh unmixing models.

	Salt Unmixing Model Means			Marsh Unmixing Model Means		
	Precision	Recall	F1 score	Precision	Recall	F1 score
Bare Soil	0.996	0.997	0.999	0.997	1	0.999
Crops	1	1	1	1	1	1
Marsh	0.999	1	0.999	0.999	0.999	1
Salt	0.991	0.988	0.989	0.998	0.976	0.987
Water	1	0.998	0.999	1	1	1

Table 3
K-fold accuracy values for salt and marsh unmixing models.

Folds	Accuracy - Salt	Accuracy - Marsh
Fold 1	0.996	0.999
Fold 2	0.998	0.999
Fold 3	1.0	0.999
Fold 4	0.996	0.999
Fold 5	1.0	0.999
Mean Accuracy	**0.998**	**0.999**

Table 4
Error matrix values from the validation of salt and marsh unmixing model outputs.

Parameter	Salt (227 points)	Marsh (761 points)
MSE	0.035	0.003
MAE	0.059	0.013
RMSE	0.186	0.054
R-square	0.50	0.90

4.1.2. RF model performance and sensitivity assessment with half-data

A similar statistical analysis was conducted for two additional sets of RF models, half-data models, trained with only half of the original input data. These models predicted a total area of 16.34 km^2 for salt patches and 1256.71 km^2 for marsh, surpassing the estimates obtained from the all-data models. The two sets of ten RF classifiers for the half-data models achieved an average training and testing accuracies of 100 % and 99.6 % for salt patches and 100 % and 99.9 % for marshes, respectively. The average testing accuracy for the half-data salt model exhibited a decrease of 0.2 % compared to the all-data salt model. However, there was only a minimal reduction in the performance metric values for the bare soil, salt, and marsh classes in the half-data salt models. The average training and testing accuracy remained unchanged for the half-data and all-data marsh models. There was a slight decrease in the metric values for bare soil and salt in the half-data marsh model, whereas the metric values for the marsh class demonstrated an increase from 0.999 to 1, specifically for precision and recall (Table 5).

4.2. Variable importance factor

The VIF analysis revealed the blue band to be the most important for salt patch classification. Notably, the two new indices introduced in this study, the Modified Salt Patch Index (MSPI) and the Normalized Difference Salt Patch Index (NDSPI), demonstrated a high level of contribution to both salt and marsh model accuracy, ranking among the top five variables alongside the blue band, EVI, and MSAVI (Fig. 6).

The salt and marsh unmixing models exhibited the same top five variables with the highest importance (Fig. 6). The blue band and EVI were the top 2 variables, while MSAVI, NDSPI and MSPI closely followed but interchanged their positions. The sharp drop in VIF for the fifth variable in the marsh model (MSPI) suggests its lower dependency on it compared to the salt model. The variables after the fifth top variable including SWIR 1, Red, Green, NIR, MSI, Red-Edge 1 and Red-Edge 2 have similar VIF's for salt and marsh unmixing.

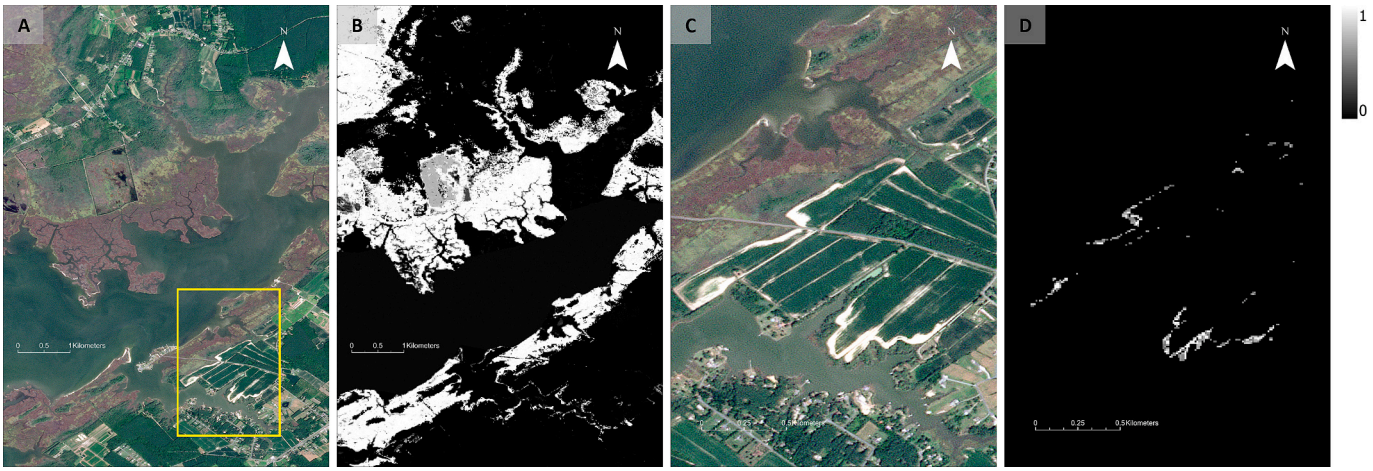

Fig. 5. The figure displays a coastal landscape in Somerset County, Maryland: (A) True color PlanetScope image. (B) Spectrally unmixed marsh layer derived from Sentinel-2 imagery with bright white color indicating 100 % marsh cover, shades of gray indicating partial marsh coverage, and black indicating less than 25 % marsh within a pixel (shown in the grayscale bar in top-right corner). (C) Zoomed-in view of the yellow box in panel A, displaying PlanetScope image of farmland severely affected by saltwater intrusion. (D) Spectrally unmixed salt patch layer for panel C landscape derived from Sentinel-2 imagery with bright white color indicating 100 % salt patch cover, shades of gray indicating partial coverage, and black indicating less than 40 % salt patch within a pixel. (For interpretation of the references to color in this figure legend, the reader is referred to the web version of this article.)

Table 5
Mean precision, recall, and F1 score from 10 models for salt and marsh unmixing performed with half the original data.

	Salt Unmixing Model (Half-Data) Means			Marsh Unmixing Model (Half-Data) Means		
	Precision	Recall	F1 score	Precision	Recall	F1 score
Bare Soil	0.995	0.992	0.991	0.996	0.995	0.997
Crops	1	1	1	1	1	1
Marsh	0.998	1	0.998	1	1	1
Salt	0.974	0.976	0.973	0.98	0.984	0.982
Water	1	1	1	1	1	1

The wide range of VIF values for variables such as NDSPI (0.075–0.170) and EVI (0.124–0.172) in the salt model reflects the inherent variability in the training and testing subsets and the random nature of the random forest algorithm, such as feature selection and decision splits. To mitigate potential bias caused by this variability, we averaged the spectral unmixing results across the ensemble of RF models and reported the standard deviation around the mean, ensuring representation of robust model performance across the predicted values.

4.3. Uncertainty analysis

Fig. 7 illustrates the standard deviation of fractional abundance predictions versus the mean of fractional abundance predictions across 10 models with randomized input data for the all-data and half-data salt and marsh unmixing models. Each scatterplot was divided into four clusters using k-means clustering, grouping pixels with similar mean values of predicted fractional abundance from 10 models. The plots show that pixels exhibiting a higher mean value of fractional abundance for salt had lower standard deviation values, and a narrower spread (Fig. 7). This indicates that the models have more certainty for the higher salt fraction prediction. Conversely, pixels with lower mean value of fractional abundance for salt and marsh exhibited higher standard deviation values and a wider spread, indicating less certainty for lower fraction prediction. Furthermore, for marsh fractional abundance values below 0.6, the standard deviation exhibited a wider range (0.03–0.22) (Fig. 7C) compared to that of salt fractional abundance values below 0.6 (0.03–0.17) (Fig. 7A). Notably, a narrower standard deviation range was evident across the half-data salt and half-data marsh models for lower fractional abundances than the all-data models.

A more pronounced negative Pearson correlation was identified

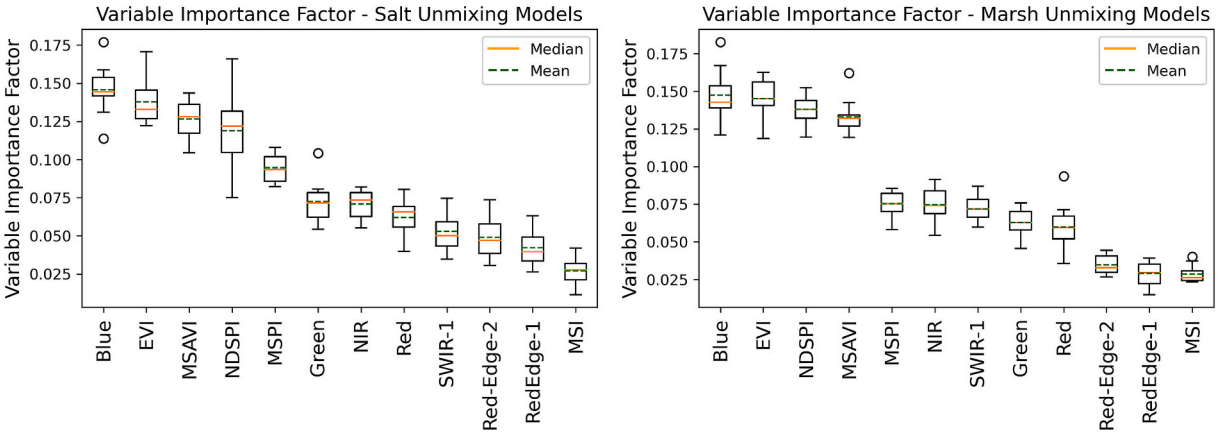

Fig. 6. Box plot illustrating the mean, median and quartile ranges (25 % and 75 %) of the Variable Importance Factor for all bands and indices used in spectral unmixing across all salt and marsh unmixing models. Bands and indices with higher importance values indicate their significant contribution to enhancing the Random Forest model's accuracy by effectively distinguishing spectral signatures associated with salt patches and marsh vegetation.

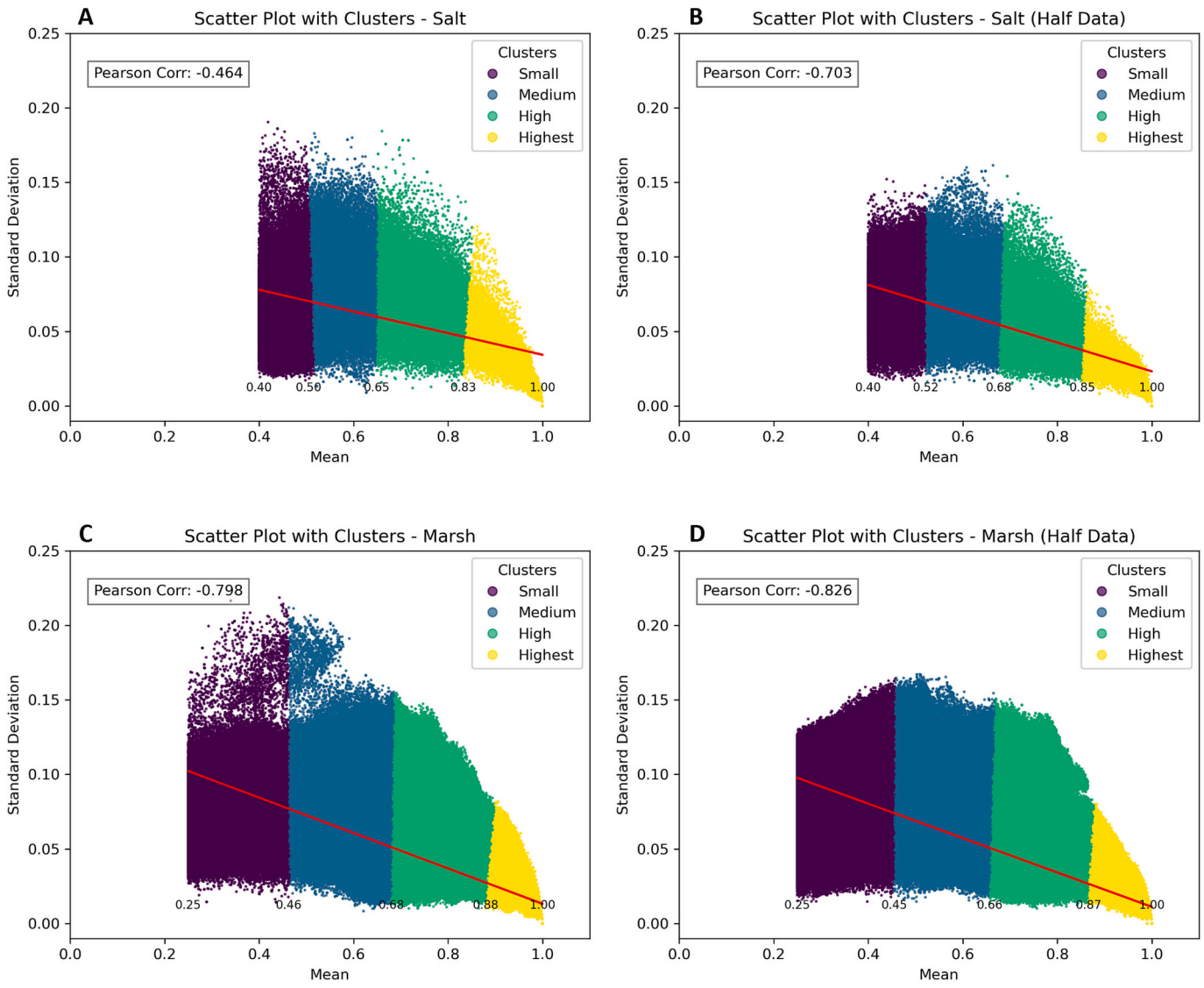

Fig. 7. Clustered scatter plot of pixels with (A) Predicted salt abundance ≥40 % using all data, (B) Predicted salt abundance ≥40 % using half of the data, (C) Predicted marsh abundance ≥25 % using all data, (D) Predicted marsh abundance ≥25 % using half of the data. Clusters were constructed using the k-means clustering algorithm with the title 'Small', 'Medium', 'High', 'Highest' based on the magnitude of mean values of fractional abundance. The fractional number close to the bottom of the scatter plot shows the start and end mean value of the cluster on x-axis. The line in red represents the linear regression line with the Pearson correlation enclosed in the top-left box for each plot. Pixels with higher mean fractional abundance for salt and marsh show lower standard deviation values and narrower spreads, reflecting greater certainty in model predictions. In contrast, lower mean fractional abundances show higher standard deviations and wider spreads, indicating less certainty. (For interpretation of the references to color in this figure legend, the reader is referred to the web version of this article.)

between the mean and standard deviation estimates in the half-data models: −0.703 (Fig. 7B) for salt and − 0.826 (Fig. 7D) for marsh unmixing models, in contrast to −0.464 (Fig. 7C) and − 0.798 (Fig. 7D), respectively, obtained from the full-data models. Each pixel is categorized into one of the four categories: 'Small', 'Medium', 'High', and 'Highest' using k-means clustering, based on the magnitude of mean values (Fig. 7). The deliberate choice of four categories facilitates ecological interpretation by effectively representing the fractional abundance of salt patches or marshes while maintaining clarity. This structured classification captures critical variability in spatial patterns, making the findings more relevant for land management and conservation efforts. For Marsh models, the approximate fractional abundance ranges are categorized as follows: 'Small' (0.25–0.45), 'Medium' (0.46–0.67), 'High' (0.68–0.87), and 'Highest' (0.88–1). For Salt models, the ranges are: 'Small' (0.4–0.51), 'Medium' (0.52–0.67), 'High' (0.68–0.84), and 'Highest' (0.85–1). This finding can be attributed to a higher number of pixels with high standard deviation in the 'Small' and 'Medium' clusters in the half-data category for both the salt and marsh (Fig. 8). An evident difference was noticed in the correlation values between the all-data salt unmixing model (−0.464) and the half-data salt unmixing model (−0.727). This is due to the larger number of pixels (120,791) assigned to the 'High' category of the half-data model compared to the number of pixels (44,508) in the 'High' category of the all-data model. Consequently, this difference contributed to a steeper negative slope in the correlation analysis.

5. Discussion

SWI is a globally escalating problem with several negative consequences (Hassani et al., 2021; Herbert et al., 2015; White et al., 2022). This study presents a novel and efficient geospatial method for mapping salt patches and marshes at a larger geographic scale, while simultaneously generating high-resolution information at sub-pixel level. Leveraging readily available Sentinel-2 imagery alongside a well-

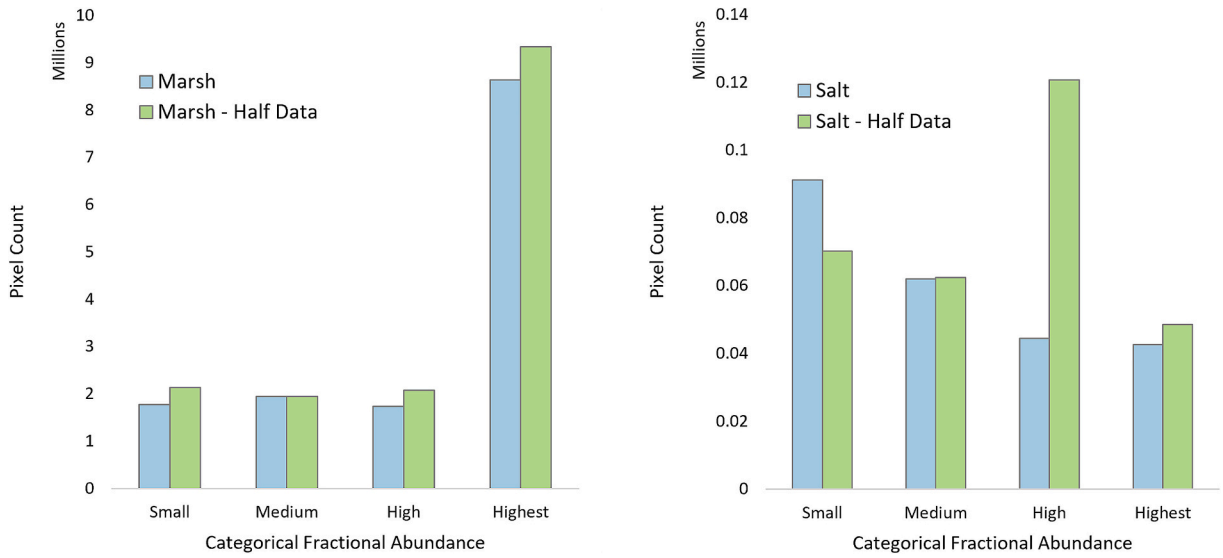

Fig. 8. Pixel count in each cluster for marsh (all data) and marsh (half-data), salt (all data), and salt (half-data). The categories: 'Small', 'Medium', 'High' and 'Highest' refer to a certain range of fractional abundance defined by the clusters in Fig. 7. For Marsh models, the approximate fractional abundance ranges are: 'Small' (0.25–0.45), 'Medium' (0.46–0.67), 'High' (0.67–0.87), 'Highest' (0.88–1). For Salt models, the approximate fractional abundance ranges are: 'Small' (0.4–0.51), 'Medium' (0.52–0.67), 'High' (0.67–0.84), 'Highest' (0.85–1).

established RF machine learning algorithm, we performed non-linear spectral unmixing to produce land cover information at the sub-pixel level. Additionally, we introduced two novel indices, NDSPI and MSPI, that enhanced the spectral unmixing process. These two indices ranked among the top five out of 12 input variables based on their evaluation using VIF. The VIF analysis revealed that the blue band made the most substantial contribution to the model's performance, consistent with a previous study by (Metternicht and Zinck, 2003), that reported a high reflectance of the blue band in the visible range for salts in soil with low moisture content. The RF classifiers achieved a high-level of training and testing accuracies—100 % and 99.8 % for capturing salt patch signatures, and 100 % and 99.9 % for classifying marshes, respectively. Other model accuracy parameters and performance metrics showcased multiple strengths and shortcomings of the method.

The slightly lower values of precision and recall for bare soil and salt class of the salt unmixing model can be attributed to the relatively small sample size of the salt class in the training and testing datasets. Additionally, the similarity in spectral signatures between pixels containing salt patches partially mixed with bare soil and pure bare soil pixels, which exhibit substantial reflectance variations, might contribute to the lower performance metrics for bare soil and salt values. This can be improved by including more samples of pure salt patch pixels as well as including more spectrally diverse pixels of bare soil in the training data that can potentially train these models to identify different spectral responses of a bare soil pixel based on its texture, crop residue on soil surface, organic matter content, surface roughness, particle size, and moisture. The lower R-squared value of 0.50 for the salt unmixing validation can result from multiple possible factors, including the inherent noise in the input data. It is important to note that only 227 points were chosen randomly to validate the salt unmixed layer visually. Salt patch misclassification can be attributed to several factors: (1) spectral similarity between white built structures (e.g. crop tunnels or building roofs) and salt patch, (2) the model's potential reliance solely on spectral information, neglecting spatial context, and (3) inadequately representative endmember spectra for salt in model training. Despite their limited number, outliers like a misclassified salt patch pixel, can significantly impact model performance. However, low values of MAE, MSE, and RMSE indicated good overall performance of the models. It is noteworthy that the models are trained with pure pixels and have no information on a mixed pixel characteristic. The same is evident in any single model's performance with the increasing standard deviation of mean predicted values categorized from 'Highest' to 'Small' fractional abundance for both salt and marsh models. The standard deviation for the categories can be reduced by providing the model with input training data of mixed pixels with targeted fractional abundance values of multiple land cover classes in that pixel. The challenge is obtaining a reliable training data set of mixed pixels and ample volume to train a machine learning algorithm to produce what is observed in nature as truly as possible.

Unsurprisingly, the all-data salt unmixing model reveals a decreasing trend in the number of pixels within the 'Small' to 'Highest' fractional abundance categories for the salt class. This aligns with the physical appearance of salt patches on farmlands, often spreading out from a nucleus. Moving away from the core of a pure salt patch pixel or a cluster of them, the pixel fraction covered with salt diminishes in all directions, resulting in varying shapes. Consequently, as one moves further from the core, the area of the salt patch expands, encompassing a larger number of pixels with lower fractional abundance of salt. In contrast, for marsh areas, most pixels are observed in the 'Highest' category of fractional abundance. This is because marshes occupy the landscape continuously, with relatively fewer pixels in the 'Small', 'Medium', and 'High' categories, primarily located at the marsh boundaries. Our model results accurately reflect the observed patterns of salt patches and marshes in the study landscape because the training dataset effectively represents the diverse range of pixel variations found across the region during the summer months.

The half-data models demonstrated similar performance metrics for salt and marsh classes as the all-data models. This could be due to the consistently good quality of the input data used for training and testing for both models. While the half-data salt unmixing model showed comparable performance for the salt class to the all-data salt model, it significantly classified more pixels in the 'High' category of salt fractional abundance, thus predicting larger areas for salt patches than the all-data model estimates. This could be due to the lack of more training data points representing pure salt pixels across the study area. Therefore, building a training dataset by incorporating a more diverse range of spectral reflectance data for pure pixels of each land cover class is crucial. It is equally important to consider the timing and environmental conditions during which the data were collected to train the model, as these factors directly dictate the model's capability to produce

generalizable output beyond any particular time or space.

Although the analysis in this study focuses on the peak of the growing season using the NDVI maximum composite from the summer months, the methodology is robust and can be applied to any time period. However, obtaining high-quality training data tailored to the specific study goal is crucial for determining the model's applicability and interpretation. For instance, to apply this methodology on images acquired throughout the year, the training dataset must account for seasonal variations in the spectral signature profiles of each land cover class. Visible salt patches, for example, may exhibit different spectral signatures during dry periods compared to wet periods and the crop cover changes over growing season, potentially leading to different results regarding the extent of observed salt patches across the study area.

The spatial extent of salt patches over agricultural land in Delmarva escalated over time, growing from around 4.72 km^2 between 2011 and 2013 to nearly doubling at 9.05 km^2 in 2016–2017 (Mondal et al., 2023). The current study reveals approximately 3-times increase in visible salt patches to 14.43 km^2 in 2022. Additionally, our findings indicate a total area of 1119.6 km^2 to be covered by marshes in Delmarva, which is an underestimation given that we masked out croplands for the marsh models.

While the presence of identifiable salt patches strongly indicates high salinization levels on farmlands, the absence of these patches may not conclusively signal the absence of salinization (Mondal et al., 2023). The temporary nature of visible salt patches is influenced by factors such as precipitation, farming practices, and regional climate (Gardner et al., 1992; Tully et al., 2019b). Despite the Delmarva Peninsula experiencing relatively high annual rainfall of approximately 1140 mm, the proximity of the water table to the surface can hinder salt dilution and transport, resulting in persistent salinity issues (de la Reguera et al., 2020; Domagalski et al., 2001). While prior studies have documented other SWI impacts such as ghost forest expansion, cropland-to-marshland conversion (Kirwan and Gedan, 2019; O'Donnell et al., 2024; White and Kaplan, 2017), the transient nature of these salt patches has hindered effective high-resolution spatiotemporal monitoring of their evolution. Our method addresses this challenge and establishes a reproducible baseline for tracking the spatiotemporal dynamics of SWI and offers high transferability to diverse coastal regions beyond the Delmarva Peninsula. The methodology proposed in this study further enhances our ability to map the impacts of SWI more accurately by building empirical models based on spatiotemporal correlations of hydroclimatic drivers such as precipitation and evapotranspiration (Hassani et al., 2021), physical and biological properties of soil (Mazhar et al., 2022; Weissman and Tully, 2020), geologic features (Goebel et al., 2017), water table levels (Guimond and Michael, 2021; Michael et al., 2013) and role of artificial drainage infrastructure such as canals, ditches, and drains (Bhattachan et al., 2018). Such a methodology is particularly important since the escalating impact of SWI is anticipated to decrease crop yields in affected areas in the upcoming years (Ullah et al., 2021; Zörb et al., 2019), negatively impacting food security and the US economy (Banerjee et al., 2018; Mondal et al., 2023).

Overall, this research contributes to the geospatial monitoring of coastal landscapes impacted by SWI. By reducing dependence on lab-derived soil salinity values, our methodology offers a scalable approach that produces high-resolution near-real-time information through the RF model. Utilizing publicly available Sentinel-2 data and Python programming enables a time- and resource-efficient implementation, allowing for monitoring over larger geographic areas with sub-pixel information at a spatial resolution of 10 m and a temporal resolution of 5 days. This capability not only enhances our understanding of SWI impacts but also has practical implications for environmental policy and agricultural management practices. By providing timely and accurate data on saltwater intrusion, this study can help local communities preserve agricultural productivity and protect livelihoods. Farmers and land managers can leverage these findings to make informed decisions regarding crop selection, irrigation practices, and soil management, ultimately enhancing resilience of coastal ecosystems to the adverse effects of SWI.

6. Conclusion

We found that the multispectral Sentinel-2 data combined with the RF machine learning algorithm can be successfully used to monitor the impacts of SWI without using lab-tested soil salinity data. We mapped salt patches and marshes at a 10 m spatial resolution, providing detailed sub-pixel information on land cover extent across the Delmarva Peninsula. The fundamental pillars of this approach include: 1) using Sentinel-2 data to capture data at high spatial and temporal scales; 2) developing two novel indices that capture the presence of a salt patch more discreetly; 3) performing non-linear spectral unmixing using the robust RF machine learning method; 4) quantifying uncertainty associated with the model prediction.

Using publicly available Sentinel-2 data, without relying on a large number of salinity values derived from soil samples, allows for a time- and resource-efficient implementation of this method. Additionally, this approach is scalable, enabling the monitoring of SWI impacts over larger geographic regions with a high spatial resolution of 10 m and a temporal resolution of 5 days. The effectiveness of this method largely depends on the quality of the training data, requiring a robust set of pure pixels that capture the diverse spectral signatures of different land covers in the study area.

It is crucial to note that mapping salt patches directly measures areas with negligible plant growth. These areas do not contribute to economic crop production or offer ecosystem services like carbon sequestration. Therefore, developing a method to promptly capture the visible consequences of this threat in near real-time holds immense potential for landscape-level monitoring and policymaking.

Supplementary data to this article can be found online at https://doi.org/10.1016/j.rse.2025.114642.

CRediT authorship contribution statement

Manan Sarupria: Writing – original draft, Visualization, Validation, Methodology, Investigation, Formal analysis, Data curation, Conceptualization. **Rodrigo Vargas:** Writing – review & editing, Supervision, Methodology, Funding acquisition. **Matthew Walter:** Writing – review & editing, Resources. **Jarrod Miller:** Writing – review & editing, Resources, Funding acquisition. **Pinki Mondal:** Writing – review & editing, Supervision, Project administration, Methodology, Funding acquisition, Conceptualization.

Declaration of competing interest

The authors declare that they have no known competing financial interests or personal relationships that could have appeared to influence the work reported in this paper.

Acknowledgements

This work was supported by the National Aeronautics and Space Administration EPSCoR Grant DE-80NSSC20M0220 awarded to P.M. and R.V. We acknowledge the financial support provided to P.M., M.W., and J.M. by the US Environmental Protection Agency (Assistance Agreement no. CB96358101), USDA Natural Resources Conservation Service (Assistance Agreement no. NR193A750007C005) and the National Fish and Wildlife Foundation's Chesapeake Bay Stewardship Fund (grant 0603.20.071142), as well as the State of Maryland and Harry R. Hughes Center for Agro-Ecology. We are grateful for the logistical support provided by the Eastern Shore Land Conservancy and Dr. Kate Tully's research group at the University of Maryland during field data collection.

Data availability

The fractional abundance datasets for salt patch and marsh produced in this study are available in Sarupria et al., 2025.

References

Adams, J.B., Smith, M.O., Johnson, P.E., 1986. Spectral mixture modeling: a new analysis of rock and soil types at the Viking Lander 1 site. J. Geophys. Res. 91, 8098–8112. https://doi.org/10.1029/JB091iB08p08098.

Alqasemi, A., Ibrahim, M., Al-Quraishi, A., Saibi, H., Al-Fugara, A., Kaplan, G., 2021. Detection and modeling of soil salinity variations in arid lands using remote sensing data. Open Geosci. 13, 443–453. https://doi.org/10.1515/geo-2020-0244.

Amini, S., Ghadiri, H., Chen, C., Marschner, P., 2016. Salt-affected soils, reclamation, carbon dynamics, and biochar: a review. J. Soils Sediments 16. https://doi.org/10.1007/s11368-015-1293-1.

Atkinson, P.M., Foody, G.M., 2002. Uncertainty in remote sensing and GIS: Fundamentals. In: Uncertainty in Remote Sensing and GIS. John Wiley & Sons, Ltd., pp. 1–18. https://doi.org/10.1002/0470035269.ch1

Bai, L., Wang, C., Zang, S., Zhang, Y., Hao, Q., Wu, Y., 2016. Remote sensing of soil alkalinity and salinity in the Wuyu'er-Shuangyang River basin, Northeast China. Remote Sens. 8 (2), 2. https://doi.org/10.3390/rs8020163.

Banerjee, S., Samanta, S., Chakraborti, P.K., 2018. Impact of climate change on coastal agro-ecosystems. In: Lichtfouse, E. (Ed.), Sustainable Agriculture Reviews 33 (Vol. 33). Springer International Publishing, pp. 115–133. https://doi.org/10.1007/978-3-319-99076-7_4.

Bannari, A., El-Battay, A., Bannari, R., Rhinane, H., 2018. Sentinel-MSI VNIR and SWIR bands sensitivity analysis for soil salinity discrimination in an arid landscape. Remote Sens. 10 (6), 6. https://doi.org/10.3390/rs10060855.

Belgiu, M., Drăguţ, L., 2016. Random forest in remote sensing: a review of applications and future directions. ISPRS J. Photogramm. Remote Sens. 114, 24–31. https://doi.org/10.1016/j.isprsjprs.2016.01.011.

Bhattachan, A., Emanuel, R., Ardon, M., Bernhardt, E., Anderson, S., Stillwagon, M., Ury, E., BenDor, T., Wright, J., 2018. Evaluating the effects of land-use change and future climate change on vulnerability of coastal landscapes to saltwater intrusion. Elem. Sci. Anth. 6, 62. https://doi.org/10.1525/elementa.316.

Blagec, K., Dorffner, G., Moradi, M., & Samwald, M. (2020). A Critical Analysis of Metrics Used for Measuring Progress in Artificial Intelligence ArXiv, abs/2008.02577. Doi:10.48550/arXiv.2008.02577.

Boardman, J.W., 1994. Geometric mixture analysis of imaging spectrometry data. In: Proceedings of IGARSS '94–1994 IEEE International Geoscience and Remote Sensing Symposium, 4, pp. 2369–2371. https://doi.org/10.1109/IGARSS.1994.399740.

Bouaziz, M., Hihi, S., Chtourou, M., Osunmadewa, B., 2020. Soil salinity detection in semi-arid region using spectral unmixing, remote sensing and ground truth measurements. J. Geogr. Inf. Syst. 12, 372–386. https://doi.org/10.4236/jgis.2020.124023.

Breiman, L., 2001. Random forests. Mach. Learn. 45, 5–32. https://doi.org/10.1023/A:1010933404324.

Campbell, A.D., Fatoyinbo, L., Goldberg, L., Lagomasino, D., 2022. Global hotspots of salt marsh change and carbon emissions. Nature 612, 701–706. https://doi.org/10.1038/s41586-022-05355-z.

Ceccato, P., Flasse, S., Tarantola, S., Jacquemoud, S., Grégoire, J.-M., 2001. Detecting vegetation leaf water content using reflectance in the optical domain. Remote Sens. Environ. 77 (1), 22–33. https://doi.org/10.1016/S0034-4257(01)00191-2.

Chesher, A., 1991. The effect of measurement error. Biometrika 78 (3), 3. https://doi.org/10.1093/biomet/78.3.451.

Corwin, D., 2020. Climate change impacts soil salinity in agricultural areas. Eur. J. Soil Sci. 72. https://doi.org/10.1111/ejss.13010.

Corwin, D.L., Scudiero, E., 2019. Chapter one—Review of soil salinity assessment for agriculture across multiple scales using proximal and/or remote sensors. In: Sparks, D.L. (Ed.), Advances in Agronomy, vol. 158. Academic Press, pp. 1–130. https://doi.org/10.1016/bs.agron.2019.07.001.

Cruz, C., Blanco, A.C., Babaan, J., Cruz, J.A., St. Ana, R.R., Paringit, E., 2019. Linear spectral unmixing of Sentinel-3 imagery for urban land cover - land surface temperature (LST) analysis: a case study of metro Manila, Philippines. Int. Arch. Photogramm. Remote. Sens. Spat. Inf. Sci. XLII-4/W19, 141–148. https://doi.org/10.5194/isprs-archives-XLII-4-W19-141-2019.

Davis, E., Wang, C., Dow, K., 2019. Comparing Sentinel-2 MSI and Landsat 8 OLI in soil salinity detection: a case study of agricultural lands in coastal North Carolina. Int. J. Remote Sens. 40 (16), 16. https://doi.org/10.1080/01431161.2019.1587205.

de la Reguera, E., Veatch, J., Gedan, K., Tully, K.L., 2020. The effects of saltwater intrusion on germination success of standard and alternative crops. Environ. Exp. Bot. 180, 104254. https://doi.org/10.1016/j.envexpbot.2020.104254.

Domagalski, J., Xinquan, Z., Chao, L., Deguo, Z., Chi, F., Kaitai, X., Ying, L., Yang, L., Shide, L., Dewen, L., Yong, G., Qi, T., Jing, L., Weidong, Y., Shedlock, R., Knifong, D., 2001. Comparative water-quality assessment of the Hai he River Basin in the People's Republic of China and the three similar basins in the United States. US Geol. Surv. Prof. Pap. 1647.

Ennaji, W., Barakat, A., Ismail, K., El Baghdadi, M., Arioua, A., 2018. Remote sensing approach to assess salt-affected soils in the north-east part of Tadla plain, Morocco. Geol. Ecol. Landsc. 2, 1–7. https://doi.org/10.1080/24749508.2018.1438744.

Fernandez-manso, A., Fernández-Manso, O., Quintano, C., 2016. SENTINEL-2A red-edge spectral indices suitability for discriminating burn severity. Int. J. Appl. Earth Obs. Geoinf. 50, 170–175. https://doi.org/10.1016/j.jag.2016.03.005.

Gallant, A., 2015. The challenges of remote monitoring of wetlands. Remote Sens. 7, 10938–10950. https://doi.org/10.3390/rs70810938.

Gardner, L.R., Michener, W.K., Williams, T.M., Blood, E.R., Kjerve, B., Smock, L.A., Lipscomb, D.J., Gresham, C., 1992. Disturbance effects of hurricane Hugo on a pristine coastal landscape: north inlet, South Carolina, USA. Neth. J. Sea Res. 30, 249–263. https://doi.org/10.1016/0077-7579(92)90063-K.

Goebel, M., Pidlisecky, A., Knight, R., 2017. Resistivity imaging reveals complex pattern of saltwater intrusion along Monterey coast. J. Hydrol. 551, 746–755. https://doi.org/10.1016/j.jhydrol.2017.02.037.

Guimond, J.A., Michael, H.A., 2021. Effects of marsh migration on flooding, saltwater intrusion, and crop yield in coastal agricultural land subject to storm surge inundation. Water Resour. Res. 57 (2), 2. https://doi.org/10.1029/2020WR028326.

Hassani, A., Azapagic, A., Shokri, N., 2021. Global predictions of primary soil salinization under changing climate in the 21st century. *Nature*. Communications 12 (1), 1. https://doi.org/10.1038/s41467-021-26907-3.

Hastie, T., Tibshirani, R., Friedman, J.H., 2009. The Elements of Statistical Learning: Data Mining, Inference, and Prediction, 2nd ed. Springer, New York.

Hegazi, E.H., Samak, A.A., Yang, L., Huang, R., Huang, J., 2023. Prediction of soil moisture content from Sentinel-2 images using convolutional neural network (CNN). Agronomy 13, 656. https://doi.org/10.3390/agronomy13030656.

Herbert, E.R., Boon, P., Burgin, A.J., Neubauer, S.C., Franklin, R.B., Ardón, M., Hopfensperger, K.N., Lamers, L.P.M., Gell, P., 2015. A global perspective on wetland salinization: ecological consequences of a growing threat to freshwater wetlands. Ecosphere 6 (10), 10. https://doi.org/10.1890/ES14-00534.1.

Holben, B.N., 1986. Characteristics of maximum-value composite images from temporal AVHRR data. Int. J. Remote Sens. 7 (11), 11. https://doi.org/10.1080/01431168608948945.

Hossain, M.L., Li, J., 2024. Salinity challenges and adaptive strategies in salinization-affected coastal Bangladesh: implications for agricultural sustainability and water resource management. Environ. Res. Lett. 19, 114048. https://doi.org/10.1088/1748-9326/ad7edb.

Hsiao, L.-H., Cheng, K.-S., 2016. Assessing uncertainty in LULC classification accuracy by using bootstrap resampling. Sciprints. https://doi.org/10.20944/preprints201608.0214.v1.

Huete, A., Didan, K., Miura, T., Rodriguez, E.P., Gao, X., Ferreira, L.G., 2002. Overview of the radiometric and biophysical performance of the MODIS vegetation indices. Remote Sens. Environ. 83 (1), 195–213. https://doi.org/10.1016/S0034-4257(02)00096-2.

Hunt, E.R., Rock, B.N., 1989. Detection of changes in leaf water content using near- and middle-infrared reflectances. Remote Sens. Environ. 30 (1), 43–54. https://doi.org/10.1016/0034-4257(89)90046-1.

Kaplan, G., Gašparović, M., Alqasemi, A.S., Aldhaheri, A., Abuelgasim, A., Ibrahim, M., 2023. Soil salinity prediction using machine learning and Sentinel – 2 remote sensing data in hyper – arid areas. Phys. Chem. Earth, Parts A/B/C 130, 103400. https://doi.org/10.1016/j.pce.2023.103400.

Karra, K., Kontgis, C., Statman-Weil, Z., Mazzariello, J.C., Mathis, M., Brumby, S.P., 2021. Global land use / land cover with Sentinel 2 and deep learning. In: 2021 IEEE International Geoscience and Remote Sensing Symposium IGARSS, pp. 4704–4707. https://doi.org/10.1109/IGARSS47720.2021.9553499.

Keshava, N., Kerekes, J.P., Manolakis, D.G., Shaw, G.A., 2000. Algorithm taxonomy for hyperspectral unmixing. Proc. SPIE 4049, 42–63. https://doi.org/10.1117/12.410362.

Kirwan, M.L., Gedan, K.B., 2019. Sea-level driven land conversion and the formation of ghost forests. *Nature*. Climate Change 9 (6), 6. https://doi.org/10.1038/s41558-019-0488-7.

Lam, Y., Winch, P.J., Nizame, F.A., Broaddus-Shea, E.T., Harun, M.G.D., Surkan, P.J., 2022. Salinity and food security in southwest coastal Bangladesh: impacts on household food production and strategies for adaptation. Food Secur. 14, 229–248. https://doi.org/10.1007/s12571-021-01177-5.

Lee, T.H., Ullah, A., Wang, R., 2020. Bootstrap aggregating and random forest. In: Fuleky, P. (Ed.), Macroeconomic Forecasting in the Era of Big Data. Advanced Studies in Theoretical and Applied Econometrics, vol. 52. Springer, Cham. https://doi.org/10.1007/978-3-030-31150-6_13.

Li, J., Pu, L., Zhu, M., Dai, X., Xu, Y., Chen, X., Zhang, L., Zhang, R., 2015. Monitoring soil salt content using HJ-1A hyperspectral data: a case study of coastal areas in Rudong County, eastern China. Chin. Geogr. Sci. 25 (2), 2. https://doi.org/10.1007/s11769-014-0693-2.

Licciardi, G., Del Frate, F., 2010. A neural network approach for pixel unmixing in hyperspectral data. In: 2nd Workshop on Hyperspectral Image and Signal Processing: Evolution in Remote Sensing, pp. 1–4. https://doi.org/10.1109/WHISPERS.2010.5594957.

Liu, M., Li, H., Li, L., Man, W., Jia, M., Wang, Z., Lu, C., 2017. Monitoring the invasion of Spartina alterniflora using multi-source high-resolution imagery in the Zhangjiang estuary, China. Remote Sens. 9 (6), 6. https://doi.org/10.3390/rs9060539.

Mahdavi, S., Salehi, B., Granger, J., Amani, M., Brisco, B., Huang, W., 2018. Remote sensing for wetland classification: a comprehensive review. GIScience & Remote Sensing 55 (5), 5. https://doi.org/10.1080/15481603.2017.1419602.

Masoud, A., Koike, K., Atwia, M.G.E.D., El-Horiny, M.M., 2019. Mapping soil salinity using spectral mixture analysis of landsat 8 OLI images to identify factors influencing salinization in an arid region. Int. J. Appl. Earth Obs. Geoinf. 83, 101944. https://doi.org/10.1016/j.jag.2019.101944.

Massetti, A., Sequeira, M.M., Pupo, A., Figueiredo, A., Guiomar, N., Gil, A., 2016. Assessing the effectiveness of RapidEye multispectral imagery for vegetation mapping in Madeira Island (Portugal). Eur. J. Remote Sensing 49 (1), 1. https://doi.org/10.5721/EuJRS20164934.

Mazhar, S., Pellegrini, E., Contin, M., Bravo, C., Nobili, M., 2022. Impacts of salinization caused by sea level rise on the biological processes of coastal soils—a review. Front. Environ. Sci. 10. https://doi.org/10.3389/fenvs.2022.909415.

Measho, S., Li, F., Pellikka, P., Tian, C., Hirwa, H., Xu, N., Qiao, Y., Khasanov, S., Kulmatov, R., Chen, G., 2022. Soil salinity variations and associated implications for agriculture and land resources development using remote sensing datasets in Central Asia. Remote Sens. 14 (10), 10. https://doi.org/10.3390/rs14102501.

Metternicht, G.I., Zinck, J.A., 2003. Remote sensing of soil salinity: potentials and constraints. Remote Sens. Environ. 85 (1), 1. https://doi.org/10.1016/S0034-4257(02)00188-8.

Michael, H.A., Russoniello, C.J., Byron, L.A., 2013. Global assessment of vulnerability to sea-level rise in topography-limited and recharge-limited coastal groundwater systems. Water Resour. Res. 49 (4), 2228–2240. https://doi.org/10.1002/wrcr.20213.

Mondal, P., Walter, M., Miller, J., Epanchin-Niell, R., Gedan, K., Yawatkar, V., Nguyen, E., Tully, K., 2023. The spread and cost of saltwater intrusion in the US mid-Atlantic. Nat. Sustain. 1–11. https://doi.org/10.1038/s41893-023-01186-6.

Mondal, P., Walter, M., Miller, J., Epanchin-Niell, R., Yawatkar, V., Nguyen, E., Gedan, K., Tully, K., 2022. High-resolution remotely sensed datasets for saltwater intrusion across the Delmarva Peninsula [Data set]. Zenodo. https://doi.org/10.5281/zenodo.6685695.

Montanarella, L., Ed, V., Yagi, K., Krasilnikov, P., Alavipanah, S.K., Mendonça Santos, M., McKenzie, N., Ed, D., Nachtergaele, F., 2015. The Status of the World's Soil Resources.

Mougenot, B., Pouget, M., Epema, G.F., 1993. Remote sensing of salt affected soils. Remote Sens. Rev. 7 (3–4), 3–4. https://doi.org/10.1080/02757259309532180.

Navarro, G., Caballero, I., Silva, G., Parra, P.-C., Vázquez, Á., Caldeira, R., 2017. Evaluation of forest fire on Madeira Island using Sentinel-2A MSI imagery. Int. J. Appl. Earth Obs. Geoinf. 58, 97–106. https://doi.org/10.1016/j.jag.2017.02.003.

Nguyen, K.-A., Liou, Y.-A., Tran, H.-P., Hoang, P.-P., Nguyen, T.-H., 2020. Soil salinity assessment by using near-infrared channel and vegetation soil salinity index derived from Landsat 8 OLI data: a case study in the Tra Vinh Province, Mekong Delta, Vietnam. Prog. Earth Planet. Sci. 7 (1), 1. https://doi.org/10.1186/s40645-019-0311-0.

O'Donnell, K.L., Bernhardt, E.S., Yang, X., Emanuel, R.E., Ardón, M., Lerdau, M.T., Manda, A.K., Braswell, A.E., BenDor, T.K., Edwards, E.C., Frankenberg, E., Helton, A. M., Kominoski, J.S., Lesen, A.E., Naylor, L., Noe, G., Tully, K.L., White, E., Wright, J. P., 2024. Saltwater intrusion and sea level rise threatens U.S. rural coastal landscapes and communities. Anthropocene 45, 100427. https://doi.org/10.1016/j.ancene.2024.100427.

Omuto, C., Nachtergaele, F., Vargas, R., 2012. State of the Art Report on Global and Regional Soil Information: Where Are we? Where to Go?.

Pesaresi, M., Corbane, C., Julea, A., Florczyk, A., Syrris, V., Soille, P., 2016. Assessment of the added-value of Sentinel-2 for detecting built-up areas. Remote Sens. 8, 299. https://doi.org/10.3390/rs8040299.

Phiri, D., Simwanda, M., Salekin, S., Nyirenda, V., Murayama, Y., Ranagalage, M., 2020. Sentinel-2 data for land cover/use mapping: a review. Remote Sens. 12, 2291. https://doi.org/10.3390/rs12142291.

Planet Team, 2017. Planet Application Program Interface: In Space for Life on Earth. San Francisco, CA. https://api.planet.com.

Qi, J., Chehbouni, A., Huete, A.R., Kerr, Y.H., Sorooshian, S., 1994. A modified soil adjusted vegetation index. Remote Sens. Environ. 48 (2), 119–126. https://doi.org/10.1016/0034-4257(94)90134-1.

Qi, M., MacGregor, J., Gedan, K., 2021. Biogeomorphic patterns emerge with pond expansion in deteriorating marshes affected by relative sea level rise. Limnol. Oceanogr. 66 (4), 4. https://doi.org/10.1002/lno.11661.

Racoviteanu, A.E., Nicholson, L., Glasser, N.F., 2021. Surface composition of debris-covered glaciers across the Himalaya using linear spectral unmixing of Landsat 8 OLI imagery. Cryosphere 15 (9), 9. https://doi.org/10.5194/tc-15-4557-2021.

Ramos, T.B., Castanheira, N., Oliveira, A.R., Paz, A.M., Darouich, H., Simionesei, L., Farzamian, M., Gonçalves, M.C., 2020. Soil salinity assessment using vegetation indices derived from Sentinel-2 multispectral data. Application to Lezíria Grande, Portugal. Agric. Water Manag. 241, 106387. https://doi.org/10.1016/j.agwat.2020.106387.

Roy, D., 2000. The impact of misregistration upon composited wide field of view satellite data and implications for change detection. IEEE Trans.Geosci. Remote Sensing 38, 2017–2032. https://doi.org/10.1109/36.851783.

Sadeghi, M., Jones, S.B., Philpot, W.D., 2015. A linear physically-based model for remote sensing of soil moisture using short wave infrared bands. Remote Sens. Environ. 164, 66–76. https://doi.org/10.1016/j.rse.2015.04.007.

Sarupria, M., Vargas, R., Walter, M., Miller, J., Mondal, P., 2025. Fractional abundance datasets for salt patches and marshes across the Delmarva Peninsula, v1. Available at:. https://doi.org/10.5281/zenodo.14709313.

Scudiero, E., Skaggs, T.H., Corwin, D.L., 2014. Regional scale soil salinity evaluation using Landsat 7, western San Joaquin Valley, California, USA. Geoderma Reg. 2–3, 82–90. https://doi.org/10.1016/j.geodrs.2014.10.004.

Shokati, H., Mashal, M., Noroozi, A., Abkar, A.A., Mirzaei, S., Mohammadi-Doqozloo, Z., Taghizadeh-Mehrjardi, R., Khosravani, P., Nabiollahi, K., Scholten, T., 2024. Random Forest-based soil moisture estimation using Sentinel-2, Landsat-8/9, and UAV-based hyperspectral data. Remote Sens. 16, 1962. https://doi.org/10.3390/rs16111962.

Sibanda, M., Mutanga, O., Rouget, M., 2015. Examining the potential of Sentinel-2 MSI spectral resolution in quantifying above ground biomass across different fertilizer treatments. ISPRS J. Photogramm. Remote Sens. 110, 55–65. https://doi.org/10.1016/j.isprsjprs.2015.10.005.

Sitokonstantinou, V., Papoutsis, I., Charalabos, K., Arnal, A., Andrés, A., Zurbano, J., 2018. Scalable parcel-based crop identification scheme using Sentinel-2 data time-series for the monitoring of the common agricultural policy. Remote Sens. 10, 911. https://doi.org/10.3390/rs10060911.

Smith, M.O., Ustin, S.L., Adams, J.B., Gillespie, A.R., 1990. Vegetation in deserts: I. A regional measure of abundance from multispectral images. Remote Sens. Environ. 31 (1), 1–26. https://doi.org/10.1016/0034-4257(90)90074-V.

Taghadosi, M., Hasanlou, M., Eftekhari, K., 2019. Retrieval of soil salinity from Sentinel-2 multispectral imagery. Eur. J. Remote Sensing 52, 138–154. https://doi.org/10.1080/22797254.2019.1571870.

Titus, J.G., Hudgens, D.E., Trescott, D.L., Craghan, M., Nuckols, W.H., Hershner, C.H., Kassakian, J.M., Linn, C.J., Merritt, P.G., McCue, T.M., O'Connell, J.F., Tanski, J., Wang, J., 2009. State and local governments plan for development of most land vulnerable to rising sea level along the US Atlantic coast*. Environ. Res. Lett. 4 (4), 4. https://doi.org/10.1088/1748-9326/4/4/044008.

Tully, K., Gedan, K., Epanchin-Niell, R., Strong, A., Bernhardt, E., BenDor, T., Mitchell, M., Kominoski, J., Jordan, T., Neubauer, S., Weston, N., 2019a. The invisible flood: the chemistry, ecology, and social implications of coastal saltwater intrusion. BioScience 69, 368–378. https://doi.org/10.1093/biosci/biz027.

Tully, K., Weissman, D., Wyner, W., Miller, J., Jordan, T., 2019b. Soils in transition: saltwater intrusion alters soil chemistry in agricultural fields. Biogeochemistry 142. https://doi.org/10.1007/s10533-019-00538-9.

Ullah, A., Bano, A., Khan, N., 2021. Climate change and salinity effects on crops and chemical communication between plants and plant growth-promoting microorganisms under stress. Front. Sustain. Food Syst. 5. https://doi.org/10.3389/fsufs.2021.618092.

Wang, J., Ding, J., Yu, D., Ma, X., Zhang, Z., Ge, X., Teng, D., Li, X., Liang, J., Lizaga, I., Chen, X., Yuan, L., Guo, Y., 2019. Capability of Sentinel-2 MSI data for monitoring and mapping of soil salinity in dry and wet seasons in the Ebinur Lake region, Xinjiang, China. Geoderma 353, 172–187. https://doi.org/10.1016/j.geoderma.2019.06.040.

Weissman, D., Tully, K., 2020. Saltwater intrusion affects nutrient concentrations in soil porewater and surface waters of coastal habitats. Ecosphere 11, e03041. https://doi.org/10.1002/ecs2.3041.

White, E., Kaplan, D., 2017. Restore or retreat? Saltwater intrusion and water management in coastal wetlands. Ecosyst. Health Sustain. 3, e01258. https://doi.org/10.1002/ehs2.1258.

White, E., Ury, E., Bernhardt, E., Yang, X., 2022. Climate change driving widespread loss of coastal forested wetlands throughout the north American coastal plain. Ecosystems 25. https://doi.org/10.1007/s10021-021-00686-w.

Zhang, T., Wang, Z., Tang, Y., Shi, Y., Zhang, Z., 2022. Soil Salinity Mapping with Landsat 8 Oli Imagery and Random Forest Algorithm (SSRN Scholarly Paper 4119211;, 4119211. https://doi.org/10.2139/ssrn.4119211.

Zörb, C., Geilfus, C.-M., Dietz, K.-J., 2019. Salinity and crop yield. Plant Biol. 21 (S1), 31–38. https://doi.org/10.1111/plb.12884.

Update

Remote Sensing of Environment
Volume 322, Issue , 15 May 2025, Page

DOI: https://doi.org/10.1016/j.rse.2025.114710

Remote Sensing of Environment 322 (2025) 114710

Contents lists available at ScienceDirect

Remote Sensing of Environment

journal homepage: www.elsevier.com/locate/rse

Corrigendum to "Non-linear spectral unmixing for monitoring rapidly salinizing coastal landscapes" [Remote Sensing of Environment Volume 319, 15 March 2025, 114642]

Manan Sarupria [a,*], Rodrigo Vargas [b], Matthew Walter [a], Jarrod Miller [b], Pinki Mondal [a,b]

[a] Department of Geography and Spatial Sciences, University of Delaware, Newark, DE 19716, USA
[b] Department of Plant and Soil Sciences, University of Delaware, Newark, DE 19716, USA

The authors regret an error in the second bullet point of the "Highlights" section in the published article. The original statement:

"Sub-pixel estimates indicate a 3-fold increase in salt patch extent since 2017."

should correctly read:

"Sub-pixel estimates indicate a 3-fold increase in salt patch extent since 2011-2013."

DOI of original article: https://doi.org/10.1016/j.rse.2025.114642.

* Corresponding author.
E-mail addresses: manansar@udel.edu (M. Sarupria), rvargas@udel.edu (R. Vargas), mswalter@udel.edu (M. Walter), jarrod@udel.edu (J. Miller), mondalp@udel.edu (P. Mondal).

https://doi.org/10.1016/j.rse.2025.114710

Available online 19 March 2025